STRESS CORROSION CRACKING IN METAL ALLOYS EXPOSED TO ACID-SO_4^{2-} CHLORIDE TYPE GEOTHERMAL FLUIDS

Katrina B. Dacillo[1]* and Sadiq J. Zarrouk[2¥]

[1]Energy Development Corporation (EDC) – 38th Floor, One Corporate Centre Building

Julia Vargas corner Meralco Avenue, Ortigas Center, Pasig City, 1605, The Philippines

[2] Department of Engineering Sciences, University of Auckalnd, Private Bag 92019, Auckland, New Zealand

*dacillo.kb@energy.com.ph and ¥s.zarrouk@auckland.ac.nz

Keywords: *stress corrosion cracking (SCC), acid sulphate, low-pH, corrosion resistant alloys (CRA)*

ABSTRACT

Stress corrosion cracking (SCC) is a materials failure caused by the simultaneous existence of stress, susceptible material and corrosive environment. Conventional geothermal wellbores producing high temperature (T > 180 ºC) acid-SO_4^{2-} chloride fluids (pH_{ave} = 3.5) may be at risk of this damage especially when subjected to stressed condition such as intermittent shut-down and discharge activities.

This study evaluated the SCC resistance in acid-SO_4^{2-} chloride geothermal fluids of six (6) types of metal alloys (i.e. J55, L80 Type-1, N06059, R53400, S32750, N08904) for potential use as casing material in geothermal wellbores. The field exposure test was conducted for 35 days using plastically deformed U-bend coupons. SCC susceptibility was measured through the appearance of a recognizable crack. Other SCC influencing factors like integrity of passive scales, surface discontinuity manifestations, test fluids chemistry and alloy composition were also considered. The SCC damage was diagnosed through gravimetric analysis, light microscopy, coupled environmental scanning electron microscopy – energy dispersive spectroscopy (ESEM-EDS), powder X-ray diffraction (XRD) and metallographic analysis.

Field test results showed all alloys covered with passive scales of sphalerite (ZnS) possibly co-existing with galena (PbS), bornite (Cu_5FeS_4), magnetite ($Fe^{2+}Fe_2^{3+}O_4$) and pyrite (FeS_2). These were adherent, porous and likely precipitated from the geothermal fluids due to absence of Zn in the original alloy composition. J55 and L80 Type 1 carbon steels had no cracks but underwent piting and appeared the most corroded. Only S32750 and N08094 corrosion resistant alloys did not develop cracks or any surface discontinuities. Nickel base alloy N06059 acquired a crack from secondary carbide precipitation and crack growth from surrounding pits. The titanium base R53400 sustained a crack that grew either from surrounding pits or through cyclic process of film rupture, dissolution and film repair based on growth of sphalerite scales into the crack. The carbon steels and R53400 were also considered at risk of hydrogen induced cracking due to H_2S presence and production of hydrogen and chloride ions during sphalerite scale formation.

1. INTRODUCTION

1.1. SCC in the Geothermal Environment

SCC is a material failure caused by the simultaneous existence of tensile stress, susceptible material and a corrosive environment. Alloys undergo SCC in specific environments that are usually, but not necessarily, aqueous and passivating. SCC often begins with crack initiation through surface discontinuities (e.g. pits, voids, microcracks, etc.), intergranular corrosion or cathodic hydrogen formation. Cracks can grow either through anodic dissolution or through cathodic hydrogen embrittlement and progress to final failure if both thermodynamic and kinetic aspects of cracking are satisfied.

SCC is one of the corrosion problems found in metallic components exposed to geothermal environments. The cracking damage observed is usually attributed to chloride-induced SCC, sulfide-induced SCC and hydrogen-induced SCC. A survey on material damage detected in seven Japanese geothermal power plants in 1992 revealed that cracking failures constituted 20.3% in geothermal drilling facilities, 10.2% in wells and pipelines and 6.4% in well logging equipment (Kurata, et. al., 1992). Because of these failures, many studies (Lichti, et. al., 1995; Lichti, et. al., 1997; Shirmohamadi, et. al., 1998; Houser, et. al., 2010; Babler, et. al., 2013; Karlsdottir, et al., 2015) to evaluate the resistance of various construction materials that are in contact with corrosive geothermal fluids have already been conducted. The SCC tests conducted in geothermal environments relied on the presence or absence of cracks as indicators of SCC resistance.

1.2 Background of the Study

The biggest challenges in geothermal corrosion control are associated with the handling of very aggressive geothermal fluids such as those found in deep geothermal resources and those with significantly high levels of corrosive properties (e.g. acidic, superheated, hypersaline, high gas, etc.). Production wells discharging corrosive geothermal fluids such as acid-sulfate chloride water, acid-chlorine sulfate water, high salinity brine and those containing high levels of non-condensable gases (NCG) have been encountered in many fields. Technologies (such as dosing chemical inhibitors, utilization of specialized alloys, etc.) to counteract the corrosive effects of these fluids have been developed but the outcome varies from one geothermal field to another. The use of corrosion resistant alloys (CRA) is also not new to the geothermal industry. However, CRAs are expensive investments. A stringent selection process for suitable CRAs, coupled with a sound business case, is necessary to protect business.

This work focuses on SCC in the geothermal environment. Specifically, the aim is to evaluate the predisposition of selected metal alloys to SCC when exposed to corrosive acid-SO_4^{2-} chloride geothermal fluids.

To our knowledge, this is the first report field testing of SCC using CRA's in low pH geothermal fluid. However, this research builds on the experience of Nogara and Zarrouk (2015) when using flat (un-stressed) CRA's testing coupons on the same fluid.

2. METHODOLOGY

2.1. Field Testing

A field test was performed to evaluate SCC resistance of four types of metal alloys (Table 1) to acid-SO_4^{2-} chloride geothermal fluids. The test fluids came from high output geothermal well XM-02 (10-12 MWe) which produces two-phase fluids having stable enthalpy between 1500-1800 kJ/kg and water fraction of about 60%. Reservoir fluid temperature based on silica geothermometer is ~320ºC. The water phase is moderately saline (*Cl* = 5,000–6,000 ppm), acidic (pH = 3.5–3.8) and has iron concentrations above 19 ppm. The gas phase contains about 2% NCG, which is comparable to levels found in many neutral-pH wells drilled within the same geothermal field. Well XM-02 fluids have no active magmatic input and are mixtures of immature equilibrated water. It is postulated that H_2S precipitated as sulfide minerals resulted in acidic fluids entering the wellbore.

Table 1. Physical and chemical properties of the carbon steels, nickel based alloy, titanium based alloy and stainless steel metals used in the field test.

Common Name	J55	L80-Type 1	5923 HMO	Ti-Gr12	2507	904L
UNS	-	-	N06059	R53400	S32750	N08904
Description	Carbon Steel		Ni-Cr-Mo alloy	98.5Ti-0.3Mo-0.8Ni	Duplex Stainless Steel	High Alloy Low Carbon Austenitic SS
Chemical Composition (%)						
C	0.36	0.23-0.24	0.004	0.014	0.018	0.01
Mn	1.02	1.20-1.23	0.18	-	0.5	1.62
P	0.007	0.015	0.004	-	0.023	0.024
S	0.003	0.005	0.001	-	0.0003	0.001
Si	0.26	0.33-0.42	0.06	-	0.3	0.34
Cu	0.17	0.01-0.02	0.004	-	0.22	1.41
Ni	0.07	0.02	61.396	0.77	6.8	24.18
Cr	0.1	0.49-0.53	22.8	-	25.54	20.02
Mo	0.02	-	15.3	0.3	3.77	4.29
Sn	0.008	-	-	-	-	-
Nb or Cb	0.001	-	-	-	-	0.026
V	0.002		-	-	-	-
Al	0.016	0.043-0.056	0.24	-	-	-
Cs	0.0015		-	-	-	-
Ti	0.025	-	-	98.675	-	-
N	0.101	-	-	0.03	0.277	0.053
Cd	0.57	-	-	-	-	-
O	-	-	-	0.137	-	-
Co	-	-	0.001	-	-	0.23
Fe	97.2654	99.96	0.01	0.104	62.55	47.796
Hardness (HV)	-	218	179-188	197	271	140-183
Yield Strength (ksi)	63.7	89.2-89.8	54-55	61.2-65.9	-	-

The acidic geothermal fluids from well XM-02 are corrosive. Casing inspection (CIC) data of the well indicate an increase in maximum recorded penetration over time. High thinning rates of 1.9105 mm/year and 3.0629 mm/year were measured within the 0–300 m depth section and 300–600 m depth section of the wellbore, respectively. These also suggest that fluids are more aggressive at the deeper sections. Corrosion was also detected in the downstream facilities such as the wellhead tee and especially in areas where the fluid flow changes direction.

The schematic diagram of the field test set-up is shown in Figure 1. Operationally, discharged fluids from XM-02 wellbore were conveyed by a 0.41 m diameter two-phase branch line into a 1.07 m diameter two-phase header that went directly into the separator station. A 0.03 m diameter by-pass line was connected into one of the 0.03 m diameter sampling points located at the bottom of the 0.41 m diameter two-phase branch line. This was used to divert XM-02 fluids into the test spool made of a 0.10 m diameter spool of 1 m long. The fluid exited the spool through another 0.03 m diameter pipe connected to a mini-silencer that was discharged through the atmosphere.

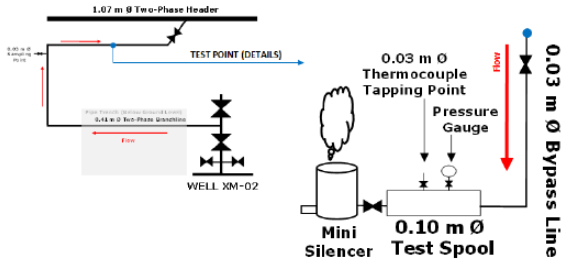

Figure 1. Schematic diagram of the field test set-up (not to scale). The size and piping lay-out of the test spool relative to XM-02 well head, two-phase branch line and header are shown.

Six types of U-bend coupons that were fabricated in accordance to ASTM G30 were used and were prepared to a surface finish of 120 grit. These were rinsed with distilled, de-ionized water, air dried and weighed to the nearest 0.01 mg based on ASTM G1-90 prior to exposure to corrosive fluids. The baseline thickness of the bent section of the U-bend coupons was also measured using a vernier caliper. The arrangement of the test coupons on the test rack and position relative to flow direction is shown in Figure 2.

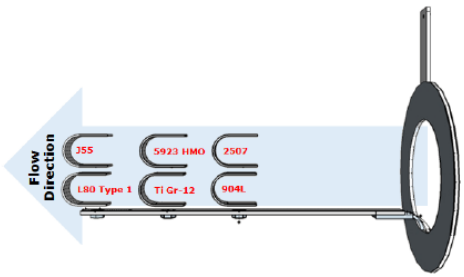

Figure 2. The six U-bend coupons mounted on the test rack and the corresponding arrangement of the specimens relative to the fluids flow and to the position of the other metal types.

The U-bend coupons were exposed to acid SO_4^{2-} chloride fluids of XM-02 for 35 days. During this period, well XM-02 was continuously operating in a fully-opened condition with well head pressure ranging from 1.33–1.40 MPa and branch line pressure between 1.18–1.21 MPa. The test spool operated at system pressure between 1.14–1.16 MPa

to maintain a fluid flow condition of 5–6 L/min. Measured fluid temperature inside the vessel was stable at 185±2 ºC.

2.2. SCC Evaluation

2.2.1. Coupon Weight and Thickness Analysis

At the end of the 35 days exposure, the test rack was immediately recovered from the test vessel after the system was successfully depressurized and drained. The U-bend coupons were dismantled and rinsed with distilled and de-ionized water to remove non-adherent debris. Thereafter, these were dried in the oven at 60 ºC for 30 minutes and allowed to cool inside a dessicator. These were then weighed individually for weight loss analysis. The thickness of the coupons, particularly at the U-bend section, was also measured using a vernier caliper for comparison with pre-exposure conditions.

2.2.2. Examination by Optical Microscopy

The U-bend coupons were scrutinized under the optical microscope prior to cleaning. The samples were viewed using a LeicaTM M80 stereomicroscope at a magnification range between 7.5× to 60× for initial detection of observable defects like pits, cracks, discoloration and textual difference. The sample images were captured and processed using an Infinity 2 USB camera and Infinity Capture imaging software (Lumenera, 2015).

2.2.3. Environmental Scanning Electron Microscopy (ESEM) and Energy Dispersive X-ray Spectroscopy (EDS)

The U-bend samples were examined through an FEI Quanta 200 F Environmental Scanning Electron Microscope (ESEM) with Energy Dispersive X-ray Spectroscopy (EDS). The ESEM was equipped with a Field Emission Gun and used an Electron Back-scatter Diffraction detector (EBSD). The voltage, spot size, magnification, detector type, working distance, pressure and temperature were specified for each scan. The EDS had a SiLi (Lithium drifted) detector with a super ultra-thin window. Genesis Spectrum software was used to identify and quantify the peaks obtained from the EDS.

ESEM–EDS were used to assess the morphology and composition of the surface deposition within the curve portion of the U-bend coupon. This was also used to check for evidence of cracking at higher magnification.

2.2.4. Powder X-ray Diffraction (XRD)

A PANalytical Empyrean X-ray Diffractometer (XRD) was used for phase identification and structural analysis of corrosion products and scales found on the surface of the U-bend coupons. A representative sample for XRD evaluation was obtained by carefully scraping off loosely adhering solids from all sections of the base metal, except the U-bend portion, to avoid inflicting any damage to the base metal. The solids were ground into fine powder with mortar and pestle. These were then mounted on clean silicon zero background sample holders for XRD analysis. The samples were scanned from a 2Θ value of 5º to 90º and diffraction results were collected using the Data Collector software. Phase identification was performed using MATCH! 3.0 software.

2.2.5. Metallographic Investigation

Two representative sections (Figure 3) were obtained from each bulk metal specimen. Section 1 was a 0.5 cm wide piece of metal cut along the U-bend curvature for cross-sectional analysis, while section 2 was a 0.5 cm × 1.4 cm piece of metal taken from within the U-bend curvature. For section 2, inspection was focused on the convex (outside) plane of the U-bend. This surface plane was stressed in tension, which typically causes SCC. A cutting wheel machine with inhibited water as coolant was used for cutting the two sections.

The sectioned samples were also mounted (3.0 cm diameter and less than 1.5 cm thick) for easier handling. These were subjected to mechanical grinding and polishing using a Struers Lavopol 21 machine. Metallographic investigations were done using light optical and electron optical microscopy. All samples were first viewed under the Olympus BX60 light microscope at 50×, 100×, 200×, 500× and 1000× magnification with a brightfield vertical illuminator. Only samples that showed evidence of cracking at 1000× magnification were examined further by ESEM-EDS. These were sputter-coated with platinum conductive coating using a Quorum Q150R S modular coating system for image enhancement.

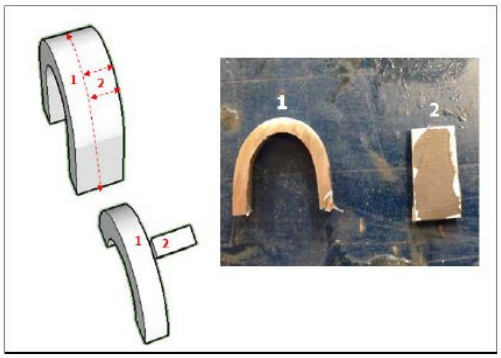

Figure 3. Diagram of where the two sections from the bulk metal of each U-bend coupon were obtained for metallographic investigations (not drawn to scale).

3. RESULTS

3.1. Results of Coupon Weight and Thickness Analysis

The surfaces of the U-bend coupons and the test rack were covered in thin black scales after 35 days exposure to acid SO_4^{2-} chloride fluids from well XM-02. The % weight gain observed among all the alloys tested was generally within 2.40–3.68% except for the Ti-Gr12 coupon which recorded the highest weight gain of 7.28%. The order in which metal alloys came into contact with the fluids did not influence the amount of solids formed on the coupon surface. Alloy 5923 HMO, which had the lowest % weight gain, and Ti-Gr12, which had the highest % weight gain, was positioned in the middle of the test rack. However, vertical placement of the coupons seemed to affect the quantity of scales formed on the metal with L80-Type 1, Ti-Gr12 and 904L coupons positioned at the bottom of the test rack having higher % weight gain than J55, 5923 HMO and 2507 coupons located at the top. This discrepancy can be attributed to non-uniform distribution of water and gas

phases within the test vessel. The bottom coupons were more exposed to a denser water phase which contained more solid particulates that could attach to the metals and serve as nucleation sites for scale formation.

All metal alloys had a comparable thickness increase within the range of 63.5–81.0% except for DSS 2507, which only had a 2.9% thickness increase. Although the thickness measurements were consistently made on the same points within the curvature of the U-bend coupons, factors such as fluid flow dynamics and phase segregation can cause scale formation or adherence within different sections of the coupons to vary. No direct relationship was established between % weight gain and % thickness increase. The alloy with the highest recorded % weight gain did not correspondingly generate the highest % thickness increase.

3.2. Results of Optical Microscope Inspection of Uncleaned Samples

Inspection of the area covered by the Teflon spacers revealed that carbon steels J55 and L80 were corroded, as manifested by the presence of rust on the surface of the base metal. A similar section on the CRA samples did not indicate corrosion but the presence of black scale was observed. This indicated that XM-02 fluids still flowed into the gap between the base metal and the spacers but only the carbon steels were corroded.

The convex side of the U-bend coupons (Figure 4) was also examined and no visible signs of cracking were found on any of the samples. Some of the black scales were chipped off from the surface of the 5923 HMO, Ti-Gr12 and 904L CRA samples but the exposed areas of the base metal did not appear to have suffered any corrosion. In contrast, the scales on the J55 carbon steel coupon were generally intact but a small area where scales were removed was corroded. Attempts to examine the concave portion of the U-bend coupons revealed that a small exposed area on the J55 sample showed the presence of black discoloration on the base metal, which could have only resulted from a reaction with the test fluids. Similar observations were not found near the concave sections of the L80 and CRA samples. No visual evidence of cracking was likewise detected.

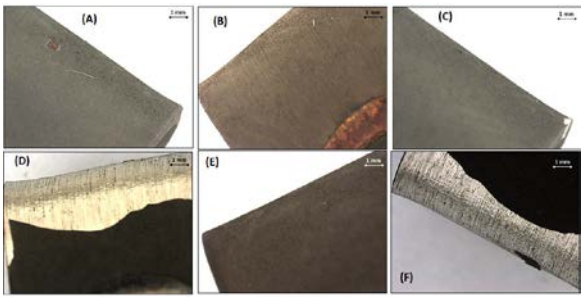

Figure 4. Images of the convex section of the uncleaned U-bend samples: (A) J55, (B) L80 Type-1, (C) 5923 HMO, (D) Ti Gr12, (E) 2507, (F) 904L.

3.3. Results of SEM-EDS Investigations on Uncleaned Samples

No evidence of cracking was found on the carbon steels since the base metal surface was generally covered with scales. The scales rendered a rough porous texture to the surface and were found to have less defined cubic crystalline morphology in irregular sizes at 4000× magnification (Figure 4, B). Elemental analysis from EDS indicated that the scale formed was mainly composed of 40–54% by weight zinc (Zn) and 23–32% by weight sulfur (S) (Figure 4, EDS 1). The calculated Zn/S mole ratio of 0.79–0.97 indicated an almost 1:1 ratio for Zn and S atoms typical of sphalerite mineral (ZnS).

The small area of exposed surface with black discoloration found on the J55 alloy was irregularly shaped with an estimated area of 500µm × 183µm. Based on EDS analysis, this was mainly composed of 44% iron (Fe), 18% O, 15% silicon (Si) and 6% C (Figure 4, EDS 2). These weight percentages translate to a Fe to O mole ratio of 1:1.5, which if reduced further can give the molecular formula for iron oxide (Fe_2O_3). A Si/C mole ratio of 1.0 was likewise obtained, which suggests the presence of silicon carbide (SiC). The surrounding area of the blackened surface was made of 59% by weight Zn and 27% by weight S (Figure 4, EDS 3).

	Elemental Weight %															
	C	O	Si	S	Cd	K	Fe	Na	Cu	Zn	Cr	Mn	Cl	As	Sb	Total
EDS 1	-	2.98	1.13	31.67	3.86	0.09	3.30	-	5.40	51.57	-	-	-	-	-	100
EDS 2	6.45	18.48	15.23	2.73	-	1.02	44.25	1.80	-	1.65	0.32	0.72	0.49	6.88	-	100
EDS 3	-	-	0.18	27.17	-	-	2.54	-	-	58.93	10.98	-	-	-	-	100
EDS 4	9.54	20.90	14.38	3.36	-	0.53	34.38	-	-	2.90	0.10	-	0.30	12.65	0.96	100

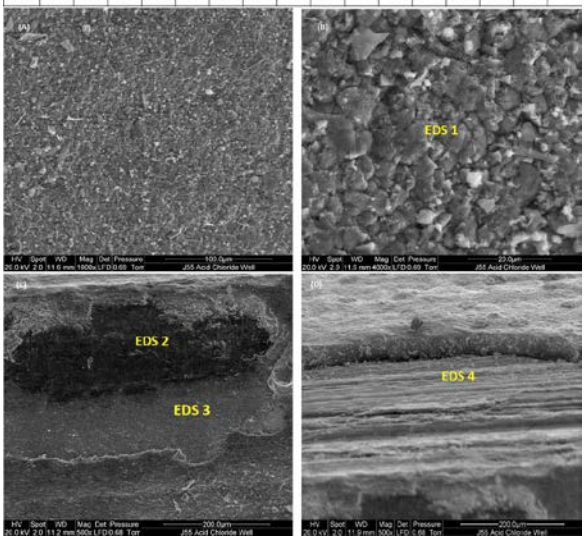

Figure 5. SEM-EDS scans on the surface of the convex section of the uncleaned J55 carbon steel U-bend sample. Images shown include surface scale at (A)1000× and (B) 4000× magnifications, (C) exposed base metal surface w/ black discoloration, (D) other sections of the base metal uncovered by flaked off scales.

The scales found on the surface of the CRA samples were also thick enough to cover any signs of damage on the base metal. However, porosity in the texture could be observed at higher magnification. SEM-EDS examinations were only made possible on the base metal surfaces of 5923 HMO, Ti Gr12 and 904L alloys because some areas on the convex section of these samples were exposed by flaked off scales. Of the three CRA samples, no visual evidence of cracking was found on the 5923 HMO sample. Results of EDS analysis also indicated that no significant alteration to the metal occurred because the weight percentages of the major components of the base metal (i.e. 58% nickel, 17% molybdenum and 22% chromium) were still comparable to

the chemical make-up of the metal before the exposure test (Table 1). However, cracking was observed on the base metal surface of the Ti-Gr 12 alloy (Figure 5, C). Some scales also appeared to be embedded inside the cracks, which were identified by EDS (Figure 5, D, EDS 4) to be mainly composed of 43% by weight Zn and 22% by weight S with a Zn/S mole ratio of 0.98. The bare Ti-Gr 12 metal surface (Figure 5, C, EDS 3) was mainly composed of 92% by weight Ti, but signatures of Zn and S were also present at weight percentages below 5%. The 904L base metal also showed seemingly branching lines on its exposed surface but no cracks with embedded scales similar to that observed in Ti-Gr12 alloys were detected. The weight percentages of major components in the 904L bare metal post-exposure to XM-02 fluids (i.e. 50% Fe, 22% Cr, 22% Ni) were also still comparable to pre-exposure conditions (Table 1) but a signature of scales composed of 46% by weight Zn and 18% by weight S was also detected.

In general, the scales found on the CRA samples were similar to those observed on the carbon steel alloys. These were mainly composed of Zn and S atoms at weight percentages ranging from 27–50% and 15–28%, respectively.

	Elemental Weight %												
	Ca	Ti	Si	S	K	Fe	Cu	Zn	O	Cd	Cl	Pb	Total
EDS 1	0.36	1.38	4.33	27.97	0.47	7.03	8.25	33.51	9.47	3.91	3.31	-	100
EDS 2	0.14	0.89	1.70	8.15	5.89	3.19	1.72	9.07	5.62	1.26	19.18	43.19	100
EDS 3	0.13	92.13	0.72	2.10	-	0.70	-	4.22	-	-	-	-	100
EDS 4	0.14	32.96	0.52	21.55	-	1.49	-	43.34	-	-	-	-	100

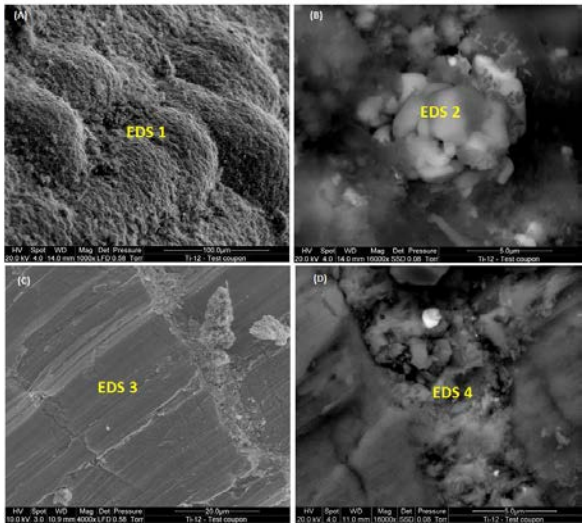

Figure 6. SEM-EDS scans on the surface of the convex section of the uncleaned Ti-Gr 12 U-bend sample: (A) scales on the surface with globular morphology at 1000× magnification, (B) round white crystalline agglomerate distributed on the scale at 16000× magnification, (C) base metal surface exposed by flaked-off scales with crack lines and (D) scales embedded in the cracks at 16000× magnification.

3.4. Results of X-ray Diffraction Analysis of Surface Scales

The diffractograms of all samples had major peaks appearing at similar 2θ values but at different peak intensities. For phase identification, the diffractograms were matched to reference patterns of six known minerals: sphalerite (ZnS), bornite (Cu_5FeS_4), magnetite ($Fe^{2+}Fe_2^{3+}O_4$), stannite (Cu_2 (Fe, Zn) SnS_4), pyrite (FeS_2) and galena (PbS). These minerals were already found present on the metal samples previously exposed to XM-02 fluids (i.e. the metal coupons used in the corrosion experiment by (Nogara and Zarrouk (2015) and the caliper tool used in the 2016 CIC survey of XM-02 wellbore (Rosell, et. al., 2016)). The chemical components of these minerals were also among the elements identified on the U-bend samples during the EDS analyses.

The analyses of diffractograms from all samples generated a 100% peak match with the reference pattern of sphalerite, a mineral that belongs to the cubic crystal system. This is consistent with the results of SEM-EDS analyses where cubic crystalline scales composed mainly of Zn and S at mole ratios approaching unity where identified. Diffractograms of scales obtained from J55 and L80 Type 1 carbon steels also had a 100% peak match for the cubic crystalline mineral galena. However, only a small amount of this mineral was likely to be present in the scales since Pb was not detected in the EDS analyses. The scales from the L80 Type 1 sample had relatively good peak matches of 88% for magnetite, 80% for moissanite (SiC) and 75% for pyrite. In contrast, scales on the J55 only had peak matches of 73% for pyrite, 62% for magnetite and 40% for moissanite. Both J55 and L80 Type 1 scale samples had 64–67% peak match with bornite and stannite.

The scales on the CRA samples did not generate 100% peak match for galena. Specifically, the percentage peak match was only 75% with the 5923 HMO scales, 80% with the Ti-Gr12 scales, 90% with the 2507 scales and 65% with the 904L scales. The peak matching with the reference patterns of the minerals bornite, magnetite, stannite and pyrite were relatively poor at less than 56% peak match for all CRA scales.

3.5. Results of Metallographic Analysis

Inspection of the section 1 cross-sectional specimens from the U-bend samples found a crack on the Ti-Gr12 alloy (Figure 7, D). The crack had a maximum width of 18µm and progressed to a maximum depth of 72µm from the convex surface of the U-bend coupon. No cracks were found on the section 1 specimens of all other samples. However, a pit of 25µm wide and 12.5µm deep was observed on the J55 carbon steel sample (Figure 7, A). The pit, which was also found on the convex surface of the sample where tensile stresses are prominent, can potentially serve as a crack initiation site on the metal.

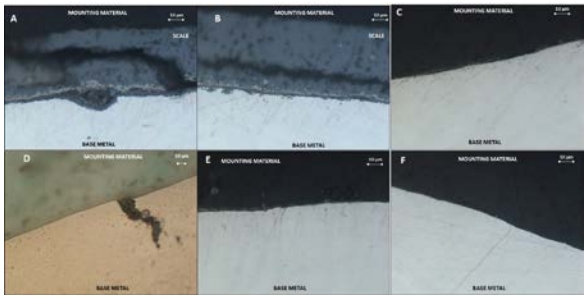

Figure 7. Metallurgical inspection of section 1 cross-sectional specimens using light optical

microscope: (A) pint on J55, (B) L80 Type 1, (C) 5923 HMO, (D) crack on Ti-Gr 12, (E) 904L.

Metallographic investigations on the Section 2 convex plane specimens from the U-bend samples revealed surface discontinuities in the form of pitting and crevice marks on the J55 and L80 Type 1 carbon steel samples. Section 2 specimens from the CRA samples showed a clean surface except for 5923 HMO and Ti-Gr12 where cracks were observed. Note that for the Section 2 specimens, grinding and polishing were performed just enough to remove the scales from the base metal.

The cracks found on the 5923 HMO and Ti-Gr12 specimens were subjected to SEM-EDS inspection. In the 5923 HMO Section 2 specimen (Figure 8), the cracks traversing the convex plane were greater than 100µm in length and had crack widths above 5µm. Pitting marks found around and within the cracks indicated that the cracks might have initiated from pits on the surface. EDS analysis performed on the crack internals showed enrichment of chromium in the metal from a pre-exposure value of 22.8% by weight to a post-exposure level of 28–59% by weight. Cr is one of the trace elements naturally found in geothermal fluids. Nearly all of the Cr remains in the geothermal brine after separation because it is a non-volatile substance. In the operating field of well XM-02, Cr levels of 10.5 µg/kg were detected on the acid SO_4-Cl fluids of an adjacent well. The EDS analyses also revealed significant depletion in the Ni and Mo contents of the metal after exposure to XM-02 fluids. The absence of Zn and S indicated that surface scale components did not embed further into the crack. Elemental C and oxygen were also present at weight percentages of 9% and 11-17%, respectively. A Cr to oxygen mole ratio of 1:1.5 was calculated, which can be further reduced to the molecular formula for chromium (III) oxide (Cr_2O_3).

	Elemental Weight %							
	Mo	O	Cr	Ni	C	Mn	Fe	Total
EDS 1	7.74	17.06	58.55	16.66	-	-	-	100
EDS 2	4.74	11.07	27.90	44.92	9.11	1.36	0.89	100

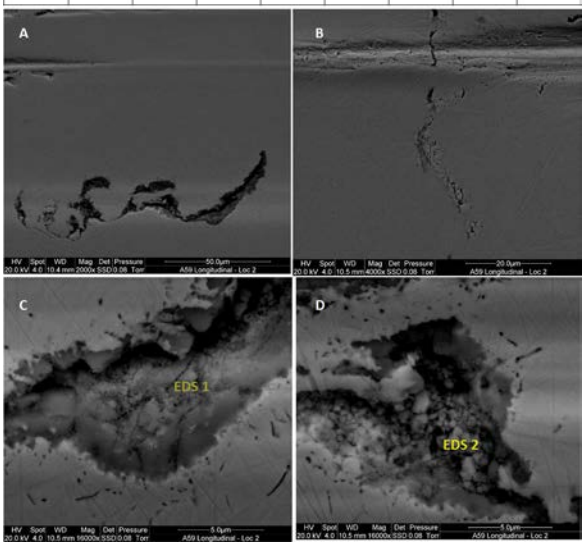

Figure 8. SEM-EDS scans on the cracks found on 5923 HMO sample. Images of the crack at (A) 2000×, (B) 4000× and 16000× (C, D) magnifications are shown.

Figure 9 shows the SEM-EDS results of the crack found on the surface of the Section 1 cross-sectional specimen from Ti-Gr12. Pitting marks were also observed around the crack but these were not as prominent as the ones found in the 5923 HMO sample. EDS analyses confirmed earlier results of scales growing into the crack because the edges of almost the entire crack length were composed of whitish materials with 21–38% by weight Zn and 9-18% S. The calculated Zn/S mole ratio of 1.0 to 1.15 was typical for sphalerite. Elemental signatures of C and oxygen atoms at weight percentages of 38–55% and 4–8%, respectively, were also detected.

	Elemental Weight %									
	C	O	Al	S	Ti	Fe	Zn	N	Si	Total
EDS 1	37.55	3.96	0.17	17.56	1.66	0.61	38.49	-	-	100
EDS 2	54.60	7.57	0.38	8.58	2.13	2.40	20.59	-	3.74	100
EDS 3	-	-	-	-	93.95	-	-	6.05	-	100

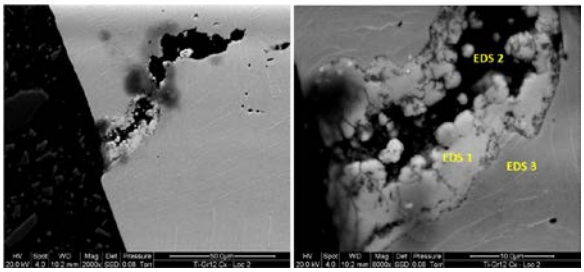

Figure 9. SEM-EDS scans on the cracks found on 5923 HMO sample. Images of the cracks at 2000× (left) and 8000× (right) magnifications.

4. DISCUSSION

The main objective of this study was to evaluate the predisposition of the selected test alloys to SCC when exposed to corrosive acid-SO_4^{2-} chloride fluids from well XM-02. The ultimate goal was to use the findings to narrow the options of suitable materials for use in wellbore and surface facilities construction. This was achieved by conducting field experiments using statically loaded smooth specimens in the form of plastically deformed U-bend test metal samples exposed to actual flowing acid-SO_4^{2-} chloride fluids in well XM-02 for 35 days. Past SCC experiments in geothermal environments have used the appearance of a recognizable crack on the test metals to measure the SCC failure of a material. This study expands the criteria to incorporate other SCC influencing factors. These include the presence and integrity of passive films, appearance of surface discontinuities on the base metal surface, metal alloy composition and test fluid chemistry.

Field test results showed that acid-SO_4^{2-} chloride fluids from well XM-02 promotes passivation in metals as manifested by weight gains and deposition of sphalerite scales on the surface of all U-bend samples exposed to the fluids. However, this finding does not necessarily imply that the metals are immune to corrosion or have no potential to fail via SCC. The degree of protection that the mineral provides to the base metal needs to be considered. Images obtained from stereomicroscope inspection of the uncleaned U-bend samples indicate uneven deposition of the scales on the metal surface. The irregular trends provided by the weight and thickness data also support initial views that phase segregation and flow dynamics inside the pipe can result in patchy deposition of scales. Hence, it cannot be discounted that uniform or localized corrosion can still occur in areas on the metal that are not yet fully covered by

scales. Note that stereomicroscope examination of the section of the uncleaned U-bend samples that was under the Teflon insulators revealed corroded base metal surfaces for J55 and L80 Type 1 carbon steels. This suggests that these metals can succumb to acid-SO_4^{2-} chloride fluids if poorly protected by sphalerite. For the CRA samples, the presence of scale and absence of rust on the metal surface under the Teflon insulators was evidence that the area had come in contact with the fluids but did not corrode.

It was noticed that sphalerite scales flaked off more readily from the surface of Ti-Gr12 and 904L alloys than in the other samples. Some portions on the surface of J55 carbon steel were also exposed due to chipped off scales. It is common for scales to detach from the metal during cooling. However, spalling or delamination of scales from the metal can also occur at any point in a corrosion process mainly because scale growth causes stress to accumulate. Large differences between the thermal expansion coefficients of the scale and the metal enhance this stress, leading to eventual detachment of scales from the surface (Khanna, 2002). It can be inferred from observations in this experiment that differences between the thermal expansion coefficients of the scale and of CRA samples Ti-Gr12 and 904L are likely to be larger in comparison to other metal samples since scales were easily detached. Note that the recurring process of cooling and heating (i.e. shut-down and start-up of geothermal wells and irregular service conditions) can cause repeated spalling and growth of scales to occur. In alloys dependent on scales for corrosion protection, repeated spalling can deplete the metal surface of elements necessary for scale growth such that the protective layer may not be completely restored (Weronski, et. al., 1991). In the case of CRAs that rely on oxide films (e.g. titanium oxide, chromium oxide), a break in the oxide layer can cause localized corrosion to occur which can serve as initiation points for SCC.

The scale formed on the surface of the U-bend metals must be properly understood in order to fully grasp its integrity as a protective scale and its overall influence on metal corrosion in the acidic fluids of well XM-02. Unfortunately, the scope of this study was limited to identifying the morphology, elemental composition and phase identity of the scales. Results of EDS and XRD analyses identified the scale as a complex matrix composed mainly of sphalerite existing in conjunction with other minerals such as galena, pyrite, magnetitie and bornite. The majority of these minerals contains elements such as Zn, S, Cu and Pb which were either not part of, or constituted only a minute amount of, the composition of the metal alloys tested. Hence, it can be inferred that scales were precipitated from the acid-SO_4^{2-} chloride fluids and deposited on the metal surface. Sulfide rich scales composed of sphalerite, galena, pyrite, chalcopyrite and bornite were also deposited in the production pipe lines of deep geothermal wells in Japan (Akaku, 1990; Yanagisawa, et. al., 2000). Albeit not well defined, a cubic crystalline morphology consistent with sphalerite mineral was generally observed on the scales of the U-bend metal samples. Images obtained from the SEM showed a rough and seemingly porous texture on the surface which could still allow fluids to pass through the relatively loose areas and into the base metal surface to cause corrosion. This probably explains why surface discontinuities in the form of pitting and crevices were still observed on the J55 and L80 Type 1 carbon steels despite the adherence of scales.

Recognizable cracks were only found on CRA samples 5923 HMO and Ti-Gr 12. The poor performance of 5923 HMO was anticipated based on pitting on the surface of the 5923HMO flat coupons previously observed by Nogara and Zarrouk (2015). SEM images of the crack showed pitting within the edges of the crack suggesting that pits might have served as crack initiation sites. EDS analysis of the crack interior showed depletion of Ni and Mo content and enrichment of C compared to the original composition of 5923 HMO before exposure. Note that in nickel-base alloys, carbon is known to precipitate carbides with Ni and Mo which can weaken grain boundaries and enhance SCC (Jones, 2003). The carbides can either be formed during the solidification process (primary) or result from thermal exposure while in service (secondary). The precipitation of secondary carbides depends on the amount of carbon in solution, exposure temperature and time at temperature (Davis, 2001). It is possible that 5923 HMO exposure to acid-SO_4^{2-} chloride fluids promoted secondary carbide precipitation. With the depletion of Mo, an element typically added to improve resistance to a non-oxidizing acid environment (Davis, 2001) such as that of well XM-02 fluids, localized corrosion such as pitting and SCC were enhanced.

The evidence for the cracking in Ti-Gr12 was found both in the uncleaned and cleaned U-bend sample. The size of the crack suggested that it was still in between the crack initiation Stage 1 and steady-state crack propagation Stage 2. It can be inferred that Ti-Gr12 did not fail by SCC after 35 days exposure to acid-SO_4^{2-} chloride fluids but the potential to fail via SCC if exposed continuously to well XM-02 fluids in the future is possible. Note that Ti alloys rely heavily on the integrity of the titanium oxide film for corrosion resistance. However, once destabilized, corrosion damage can occur very rapidly (Thomas, 2003). The high affinity of titanium metal to oxygen can promote re-healing of the titanium oxide film. This is the reason why it is the choice material for oxidizing environments but not for reducing media. Reducing acids (e.g. hydrochlorics, sulfuric, etc) often cause general corrosion on titanium alloys, the degree of which is dependent on the concentration and temperature of the media (Houser, 2010). Alloying elements such as Ni, Mo, palladium (Pd) and ruthenium (Ru) are often added to titanium to increase resistance to reducing acids.

SEM-EDS analysis of the Ti-Gr12 sample indicated sphalerite growth in the crack. Signs of pitting were also found around the crack. It is possible that the layer of titanium oxide film formed on the Ti-Gr12 surface was not stable enough given the reducing nature of the acid-SO_4^{2-} chloride geothermal fluids of well XM-02. A poor oxide layer can leave the metal susceptible to localized corrosion such as pitting particularly in areas with broken passive film. Note that pitting is often a pre-cursor to crack growth. It is also possible that stress accumulated by sphalerite scale deposition destabilized the titanium oxide layer to allow cracks to propagate by the cyclic process of film rupture, dissolution and film repair.

It is interesting to point out as well that the mechanism of sphalerite formation may also have an effect on the cracking susceptibility of Ti-Gr12. The proposed

hydrothermal reaction for sphalerite formation (Equation 1) shows a release of hydrogen and chloride ions into solution Nogara and Zarrouk (2015). Zinc ions stay in solution as metal complexes with Cl^- and HS^- ligands and precipitates as sulfide minerals when fluid temperature, pressure or pH favors the deposition process (Akaku, et. al., 1991; Nogara and Zarrouk, 2015). Note that titanium and its alloys are susceptible to hydrogen embrittlement due to the formation of hydride. Unfortunately, evidence of hydride formation within the crack could not be established since hydrogen presence cannot be detected by EDS. However, the possibility of hydrogen-induced cracking in the Ti-Gr12 metal is not discounted, especially since sphalerite deposition and H_2S presence in well XM-02 fluids have the tendency to increase exposure of the alloy to hydrogen.

$$ZnCl^+_{(aq)} + H_2S_{(aq)} \rightarrow ZnS(\text{sphalerite}) + 2H^+_{(aq)} + Cl^-_{(aq)} \quad (1)$$

Cracks and surface discontinuities were not found on the 2507 and 904L CRA samples. However, the likelihood of localized corrosion and SCC occurrence on this alloy should not be dismissed until the degree of protection that sphalerite scales can offer to the metals is fully understood. Note that in the field test done by (Nogara and Zarrouk (2015) pitting was also observed on alloy 2507. Carbon steels are also known to be susceptible to hydrogen-induced cracking in H_2S environments. Poor sphalerite scale protection puts J55 and L80 Type 1 metals at risk of hydrogen induced cracking especially since pits that can serve as initiation sites for crack growth were already detected in these alloys. The mechanism at which sphalerite scales are deposited along the XM-02 wellbore and of the scale's protective capability on the metal must be properly understood. This may do away with investing in expensive CRA's in favor of finding technologies that can reinforce the role of sphalerite scale on carbon steel integrity.

5.0 CONCLUSIONS

The metal alloys tested in acid-SO_4^{2-} chloride fluids were J55 and L80 Type 1 carbon steels, duplex stainless steel 2507 (UNS S32750), super austenitic stainless steel 904L (UNS N08904), nickel-base alloy 5923 HMO (N06059) and titanium base alloy Ti-Gr12 (R53400). The following conclusions were derived from the 35-day field exposure test:

- All alloys tested were covered with passive scales of sphalerite (ZnS) co-existing with galena, bornite, magnetite and pyrite. The sphalerite was likely precipitated from the fluids since the Zn component of the mineral was not part of the metal alloy composition. The scales have poor protective properties. These were adherent but showed a porous texture that could enable fluid to creep into the base metal surface. The same scale was reported by (Nogara and Zarrouk 2015).
- The scales formed on the Ti-Gr12 and 904L samples flaked off easily after the testing. Stress accumulation brought about by the large difference in thermal coefficients between the sulfide scale and the metals likely caused the scales to spall.
- The J55 and L80 Type-1 carbon steels did not sustain any cracks but had pits on the surface that could serve as initiation sites for crack growth. The corroded area of the base metal surface under the Teflon insulators also validated the poor corrosion resistance of these alloys to the acid-SO_4^{2-} chloride fluids. Nogara and Zarrouk (2015) also reported general and pitting corrosion underneath the scale of both (J55 and L80) carbon steels.
- The 5923 HMO nickel base CRA acquired a crack on the surface. This was caused by secondary carbide precipitation based on depletion of Mo and Ni and enrichment of C within the crack. The crack likely grew from pits observed within and around the crack. Nogara and Zarrouk (2015) did report very rare pitting which could imitate SCC.
- The Ti-Gr12 titanium base CRA sustained a crack on the base metal surface. The reducing nature of the fluid and the accumulated stress brought about by sphalerite precipitation destabilized the protective titanium oxide film. The crack possibly propagated either from pits found around the crack or through the cyclic process of film rupture, dissolution and film repair based on the growth of sphalerite scales in the crack. This is an interesting observation since it is the first time Ti-Gr12 has been reported to be tested in this low pH fluid environment. Caution is advised when considering Ti-Gr12 in such environment.
- The 2507 duplex stainless steel and 904L superaustenitic stainless steel did not develop cracks or any surface discontinuities. However, the role of sphalerite scale deposits as metal protection needs to be further investigated, since 2507 acquired pitting in its previous exposure to the acid-SO_4^{2-} chloride fluids (Nogara and Zarrouk, 2015).
- The Ti-Gr12 and carbon steel alloys are at high risk of hydrogen cracking because of the production of hydrogen and chloride ions during sphalerite formation and the presence of H_2S in the acid-SO_4^{2-} chloride fluids (equation 1).

REFERENCES

Akaku, K. (1990). Geochemical Study on Mineral Precipitation from Geothermal Waters at the Fushime Field, Kyushu, Japan. *Geothermics , 19 (5)* , 455-467. Great Britain: Pergamon Press.

Akaku, K., Reed, M. H., Yagi, M., Kai, K., & Yasuda, Y. (1991). Chemical and Physical Processes Occurring in the Fushime Geothermal System, Kyushu, Japan. *Geochem. J. (25)* , 315-333.

Babler, R., Sobetzki, J., & Klapper, H. S. (2013). Corrosion Resistance of High Alloyed Materials in Artificial Geothermal Fluids. *CORROSION 2013* . NACE International.

Davis, J. R. (2001). *Alloying: Understanding the Basics.* ASM International.

Houser, R. P. (2010). Performance of Eleven Ti Alloys in High Temperature, High Pressure Brine Solution. *Proceedings World Geothermal Congress* .

Jones, R. H. (2003). Stress Corrosion Cracking. In *ASM Handbook, Volume 13A - Corrosion: Fundamaentals, Testing and Protection.* ASM International.

Karlsdottie, S., Ragnarsdottir, K. R., Throbjornsson, I. O., & Einarsson, A. (n.d.). Corrosion Testing in Superheated Geothermal Steam in Iceland. *Geothermics , 53* , 281-290.

Khanna, A. S. (2002). Introduction to High Temperature Oxidation and Corrosion. ASM International.

Kurata, Y., Sanada, N., Nanjo, H., & Ikeuchi, J. (1992). Material Damages in Geothermal Power Plants. *Proceedings 14th New Zealand Geothermla Workshop 1992* .

Lichti, K., Johnson, C. A., Mellhone, P. G., & Wilson, P. T. (1995). *Corrosion of Iron-Nickel Base and Titanium Alloys in Aerated Geothermal Fluids.* World Geothermal Congress 1995.

Lumenera. (2015). Infinity Capture Imaging Software. Lumenera Corporation.

(Nogara and Zarrouk J., & Zarrouk, S.J. (2015) Surface Analysis of Carbon Steel and Corrosion-Resistant Alloys Exposed to Acid-SO4= Chloride Type Geothermal Fluid. Proceedings the 37th New Zealand Geothermal Workshop, 18-20 November, Taupo, New Zealand.

Rosell, J. B., & Concepcion, R. (2016). Internal Petrologic Report.

Shirmohamadi, M., Ridgely, J., & Bloomfield, K. (1998). Simulating and Monitoring of Stress Corrosion Cracking Under Geothermal Steam. *Geothermal Resource Council Transactions (22)* .

Thomas, R. (2003). Titanium in the Geothermal Industry. *Geothermics* , 679-687. Elsevier Ltd.

Weronski, A., & Hejwowski, T. (1991). Thermal Fatigue of Metals. Marcel Dekker, Inc.

Yanagisawa, N., Fujimoto, K., & Hishi, Y. (2000). Sulfide Scaling of Deep-Geothermal Well at Kakkonda Geothermal Field in Japan. *Proceedings World Geothermal Congress 2000* . Kyushu-Tohoku, Japan.